The effect of the fatigue damage accumulation process on the damping and stiffness properties of adhesively bonded composite structures

Khoshmanesh, S.; Watson, S. J.; Zarouchas, D.

DOI
10.1016/j.compstruct.2022.115328

Publication date
2022

Document Version
Final published version

Published in
Composite Structures

Citation (APA)
Khoshmanesh, S., Watson, S. J., & Zarouchas, D. (2022). The effect of the fatigue damage accumulation process on the damping and stiffness properties of adhesively bonded composite structures. *Composite Structures*, *287*, Article 115328. https://doi.org/10.1016/j.compstruct.2022.115328

Composite Structures 287 (2022) 115328

Contents lists available at ScienceDirect

Composite Structures

journal homepage: www.elsevier.com/locate/compstruct

The effect of the fatigue damage accumulation process on the damping and stiffness properties of adhesively bonded composite structures

S. Khoshmanesh [*], S.J. Watson, D. Zarouchas

Faculty of Aerospace Engineering, TU Delft, Kluyverweg 1, 2629 HS Delft, The Netherlands

ARTICLE INFO

Keywords:
Adhesive joint
Fatigue
Loss factor
Stiffness
Thermography

ABSTRACT

Wind turbine blade spar cap to shear web adhesively bonded connections can suffer from damage at the bond-line which can propagate through the structure compromising blade integrity. This study investigates changes in the stiffness and damping of a thick adhesive joint test specimen during a fatigue test. The stiffness is calculated using an extensometer and damping is determined using vibration and thermography. Fatigue tests showed three distinct phases of damage. Firstly, transverse cracks and delamination initiate and grow with little change in stiffness observed while damping increases by 18.6% and 17.8% inferred from the vibration and thermographic methods, respectively. In the second phase, the number of transverse cracks increases reaching saturation and the stiffness reduces by 4.7%. The increase in the loss factor is 65.7% and 95.6% from the vibration and thermographic methods, respectively. In the final phase, the crack density remains constant whilst de-bonding of the joint begins and grows until failure. The loss factor increases by 111.4% and 116.9% from the vibration and thermographic methods, respectively though the stiffness shows a cumulative reduction of only 8.6%. The results show the potential for monitoring changes in damping to infer incipient damage in an adhesively bonded composite joint structure.

1. Introduction

The adhesively-bonded connections in modern wind turbine blades, *e.g.* spar caps to shear webs and the leading/trailing edges, are key elements that contribute to their structural integrity. These parts suffer from damage at the bond-line which can propagate through the structure and compromise the structural integrity [1,2]. With the ever-increasing size of wind turbine blades, particularly for offshore machines with lower accessibility, deploying a health monitoring system in order to detect damage and take appropriate maintenance actions will become essential to reduce the levelized cost of energy (LCOE) [3,4]. Past research has suggested four methods for the health monitoring of a wind turbine blade [5]: vibration-based methods, strain measurements, acoustic emission and ultrasonic wave propagation. For the acoustic emission and the ultrasonic wave propagation methods, sensors should be close to the damage source in order to detect damage. Therefore, large number of sensors would need to be installed in different parts of a blade in order to effectively monitor damage, which is an expensive and impractical solution [6]. The vibration-based techniques, are easier to implement and at the same time can provide useful information related to the damage process.

In the case of vibration-based health monitoring, the methods proposed to date rely mostly on measuring changes in the stiffness of a structure to identify damage [7–11]. But in a complex structure like a wind turbine blade, which consists of several structural elements, such as spar caps, trailing and leading edges, *etc*, changes in the stiffness may not be significant unless severe damage occurs which can compromise the operation of the wind turbine [12]. One property of a composite structure which seems to be more effective than stiffness for early damage detection and its evolution is the damping.

Early experimental investigations to identify damage by measuring the damping property of a material were carried out by Modena et al. and Zonta et al. [13,14]. They evaluated the use of modal damping to identify manufacturing defects or structural damage in pre-cast reinforced concrete. In a similar fashion Kawiecki, [15] showed the feasibility of measuring modal damping by using arrays of piezoelectric transducers in a study on two types of concrete blocks. It was found that damping could be a useful property to detect damage in the structure. Keye et al. [16] also verified the concept of measuring the change in modal damping as a suitable indicator to identify damage in carbon fibre reinforced polymer (CFRP) materials. Kyriazoglou et al. [17] measured the specific damping capacity of woven glass fibre reinforced polymer (GFRP) laminate before and after the introduction of damage using quasi-static loading. The results indicated that measurement of

---

[*] Corresponding author.
E-mail address: s.khoshmanesh@tudelft.nl (S. Khoshmanesh).

https://doi.org/10.1016/j.compstruct.2022.115328
Received 16 July 2021; Accepted 27 January 2022

damping could be a promising technique for detection of initial cracks in a woven fabric composite.

Zhang et al. [18] studied the effect of fatigue damage on damping of unidirectional GFRP and CFRP laminate. They also found that a change in damping was a useful indicator to detect the formation and growth of micro cracks in these laminates.

KiRal et al. [19] investigated the effect of impact damage on the damping in a woven GFRP beam-type structure. The results showed changes to the damping ratio to be a more sensitive measure of impact damage than changes in the natural frequency. Birman et al. [20] presented an analytical method to estimate the effect of matrix cracks on damping in unidirectional and cross-ply ceramic matrix composites. The results showed that damping considerably increases with growth of the matrix cracks. Cao et al. [21] reviewed several studies using changes to damping properties as a way to detect structural damage. They concluded that a number of the studies did demonstrate that changes in damping showed greater sensitivity to damage than changes in the natural frequencies or mode shapes, but that damping-based damage identification is still a research area 'in progress' and is not yet well-established.

Kopparthi et al. [22] studied the effect of delamination on visco-elastic properties of woven GFRP laminates. They observed that the loss factor increases as a result of the delamination but its change is dependent on the size and the location of the delaminated area. Shen et al. [23] also studied the effect of delamination on the visco-elastic properties of plant fibre-reinforced composite. They concluded that delamination can greatly increase the loss factor of this type of composite material.

Changes to the damping properties of adhesively-bonded composite structures under fatigue has not had much attention to date and for this reason is the subject of this work. The work is an extension of a previous study involving measurements of changes to the damping properties of an adhesively-bonded connection during a fatigue test [24]. This study extends the work to include measurements from multiple samples, to compare changes in both stiffness and damping properties and to contrast the use of vibrometry with infrared measurements for detecting fatigue damage.

In the case of the vibration measurements, damping is estimated using a visco-elastic model of the damping appropriate for a composite material [25,26]. In the case of the thermography measurements, the damping is inferred by relating the temperature increase to the heating generated in the material.

2. Wind turbine blade structure

A wind turbine blade consists of aerodynamic shells (the pressure side and suction side) and shear webs which are moulded separately and then bonded together in an assembly process using a structural adhesive. The load carrying parts of the shells (spar caps) are constructed from uni-directional composite laminates such as thick GFRM (glass fibre-reinforced materials) [27,28].

Shear webs are built from multi-axial fibre lay-ups and a core of balsa wood or polyvinyl chloride (PVC) foam. The web body is produced by infusion of a balsa/foam core with thin skin laminates, whereas the web foot is primarily made of multi-axial direction glass fibres. The spar-web adhesive joint is manufactured by bonding the web foot onto the spar cap of the blade as shown in Fig. 1. This web adhesive joint is a key element for the structural integrity of the blade. If the joint suffers fatigue damage at the bond-line then this can propagate through the spar cap and lead to de-lamination and de-bonding of the spar cap from the webs. Early detection of such damage is important for wind turbine maintenance, but such maintenance normally requires visual inspection either from the ground or by climbing the turbine. As damage may not be visible from the outside such methods may not be reliable. Remote measurements based on vibrometry or thermography have the potential to provide more reliable information about blade damage and their use and analysis are thus the motivation for this work.

3. Theoretical background

3.1. Vibration method

Compared to metals, composite materials have generally a higher damping capacity. The main reason for this is the viscous-elasticity of the polymeric matrix [26]. In fibre-reinforced polymers, the dominant damping mechanism is related to the visco-elastic behaviour of the matrix and/or fibre materials [25]. For a linear visco-elastic material, the constitutive equation for a simple one-dimensional stress–strain relationship at time t can be written as [29],

$$\sigma(t) = \int_{-\infty}^{t} g(t-\tau)d\epsilon(\tau) \tag{1}$$

where $\sigma(t)$ is the time-dependent stress, $\epsilon(t)$ is the time-dependent strain, τ is the characteristic relaxation time and $g(t)$ is the relaxation modulus associated with the material properties. The Laplace transform of Eq. (1) can be written as,

$$\bar{\sigma}(s) = s\bar{G}(s)\bar{\epsilon}(s) \tag{2}$$

where $\bar{\sigma}(s)$, $\bar{G}(s)$ and $\bar{\epsilon}(s)$ are the Laplace transformed components of $\sigma(t)$, $g(t)$ and $\epsilon(t)$, respectively and s is the complex frequency parameter in the Laplace domain. If the strain is assumed to be harmonic with amplitude of ϵ_0 and angular frequency of ω then,

$$\epsilon(t) = \epsilon_0 e^{j\omega t}. \tag{3}$$

Then in the Laplace transformed domain,

$$\bar{\epsilon}(s) = \epsilon_0\delta(s-j\omega) \tag{4}$$

where δ is the Dirac delta function. Using the inverse definition of the Laplace transform,

$$\sigma(t) = \int_{-\infty}^{+\infty} \bar{\sigma}(s)e^{st}ds. \tag{5}$$

Substituting Eq. (2) and Eq. (4) into Eq. (5) gives:

$$\sigma(t) = \int_{-\infty}^{+\infty} s\bar{G}(s)\epsilon_0\delta(s-j\omega)e^{st}ds \tag{6}$$

which results in:

$$\sigma(t) = j\omega\bar{G}(\omega)\epsilon_0 e^{j\omega t}. \tag{7}$$

This equation relates the stress and strain for a harmonic excitation where the term $j\omega\bar{G}(\omega)$ is the dynamic modulus and is usually expressed as:

$$j\omega\bar{G}(j\omega) = E'(\omega) + jE''(\omega) \tag{8}$$

where E' is the storage term and E'' is the loss term. The loss tangent or loss factor represents the damping of the material and is defined as:

$$\tan(\delta(\omega)) = \frac{E''(\omega)}{E'(\omega)}. \tag{9}$$

The time domain equation of motion of a single beam element of a linear visco-elastic beam structure in finite element form can be written as [30]:

$$\mathbf{M}^{e}\ddot{\mathbf{y}}(t) + g(t)\mathbf{K}^{e}\mathbf{y}(0) + \int_{0}^{t} g(t-\tau)\mathbf{K}^{e}\frac{d\mathbf{y}(\tau)}{d\tau}d\tau = \mathbf{f}(t) \tag{10}$$

where $\mathbf{M}^{e}$, $\mathbf{K}^{e}$, $\mathbf{y}(\mathbf{t})$ and $\mathbf{f}(t)$ are the mass matrix, stiffness matrix (where the dynamic modulus has been factored out), displacement vector and force vector for a single element, respectively.

For a harmonic load, $\mathbf{f}(t) = \bar{\mathbf{F}}(\omega)e^{j\omega t}$, the response is also harmonic, *i.e.* $\mathbf{y}(t) = \bar{\mathbf{Y}}(\omega)e^{j\omega t}$, and Eq. (10) becomes:

$$-\omega^2\mathbf{M}^{e}\bar{Y}(\omega) + (E'(\omega) + jE''(\omega))\mathbf{K}^{e}\bar{Y}(\omega) = \bar{\mathbf{F}}(\omega) \tag{11}$$

where $\bar{\mathrm{F}}(\omega)$ and $\bar{\mathrm{Y}}(\omega)$ are the amplitude of the harmonic load and the displacement, respectively. Eq. (11), can be applied to all elements of

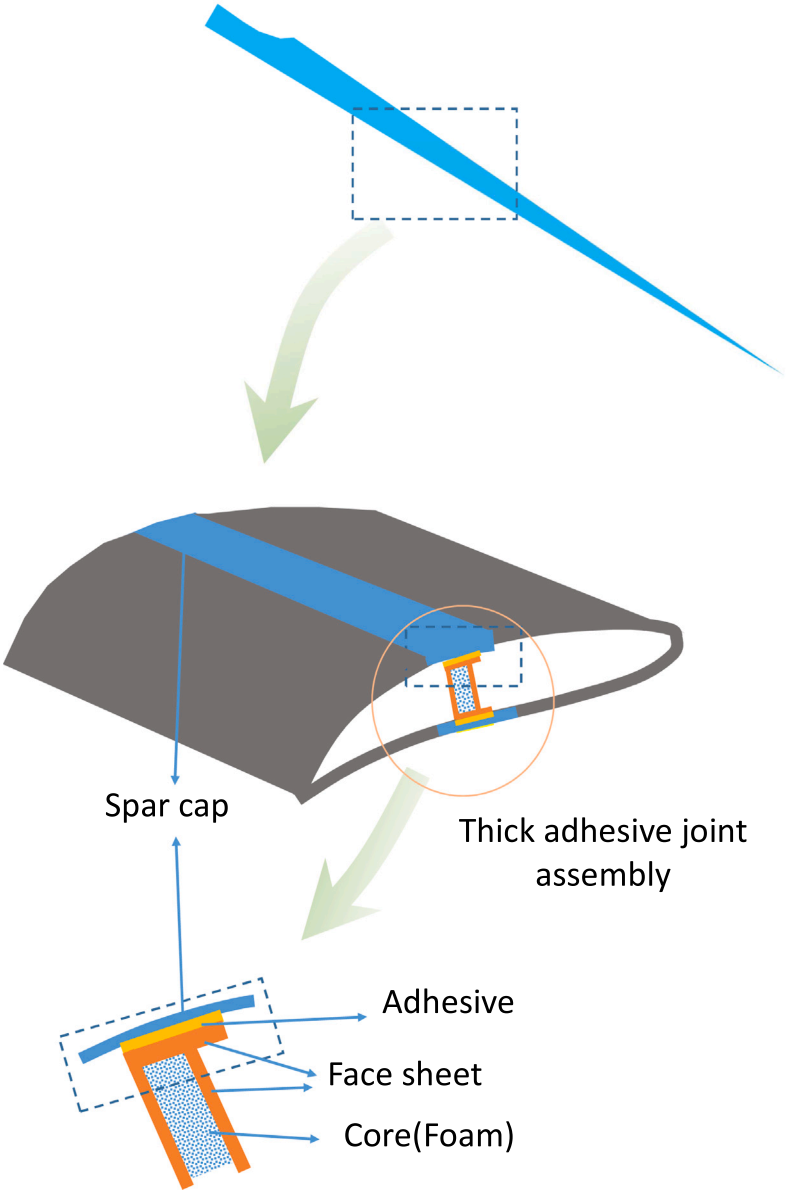

Fig. 1. Schematic illustration of a spar cap/shear web thick adhesive joint..

a beam structure and the dynamic response of a beam structure to a harmonic force can be obtained. The form of the equation for the dynamic response of the whole beam structure is the same as that for a single element (Eq. (11)) except that element terms such as $\mathbf{M}^e$, $\mathbf{K}^e$ and $\bar{\mathbf{Y}}(\omega)$ should be replaced with **M**, **K** and **Y** for the whole structure. In this case, the Frequency Response Function (FRF) for the whole structure is defined as:

$$\mathbf{FRF} = (-\omega^2\mathbf{M} + (E'(\omega) + jE''(\omega))\mathbf{K})^{-1} \tag{12}$$

where **M** and **K** are now the global mass and stiffness matrices. From Eq. (12), the analytical response of a structure in the frequency domain can be calculated. In this paper, the GHM (Golla–Hughes–McTavish) parametric form of the dynamic modulus has been used,[30]:

$$E'(\omega) + jE''(\omega) = G^0[1 + \alpha\frac{(s^2 + 2\zeta\bar{\omega}s)}{(s^2 + 2\zeta\bar{\omega}s + \bar{\omega}^2)}] \tag{13}$$

Where $s = j\omega$ and G^0, α, ζ and $\bar{\omega}$ are model parameters which are fitted to experimental data.

3.2. Thermography method

When a material is subjected to a cyclic fatigue load, energy is dissipated inside the material in the form of heat due to structural damping. This increases the temperature of the material which can be measured using a thermographic camera sensitive to infrared light. The increase in temperature can be correlated to the dissipation of energy to estimate the damping property of the material. In visco-elastic materials, the dissipation of energy due to damping during one loading cycle can be written as [31]:

$$W_d = \pi\tan(\delta)(\frac{\sigma^2}{E}) \tag{14}$$

where W_d and $\tan(\delta)$ are the dissipation of energy and loss factor respectively, E is elastic modulus of the material and σ is the stress amplitude defined by:

$$\sigma = \frac{\sigma_{max} - \sigma_{min}}{2} \tag{15}$$

where σ_{max} and σ_{min} are the maximum and minimum stress, respectively, during the fatigue tension test.

Table 1
Mechanical properties of different components for manufacturing of test specimens where: E_Y = Young's Modulus, σ_u = ultimate strength and ρ = volume density.

	Material specification		E_Y (GPa)	σ_u (MPa)	ρ (g/cm^3)
Adhesive	Resin	Epoxy Epikote Resin MGS BPR135G2	5.5	75	1.1–1.2
	Curing agent	Epoxy Epikure Curing Agent MGS BPH1355G			
Adherent	Resin	Epoxy Epikote Resin MGS RIMR135	22.8	376	1.3–1.17
	Curing agent	Epoxy Epikure Curing Agent MGS RIMH 137			0.99
	UD fibre glass	Fibre glass cloth UD (0), 1210 g/m^2, S14EU960			–

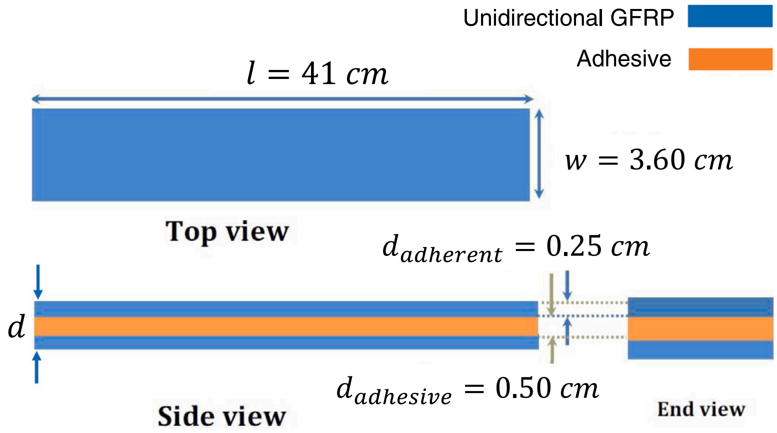

Fig. 2. Schematic illustration of a test specimen..

To correlate the dissipation of energy to the temperature T of the test specimen, the heat loss/gain within the test specimen should be considered. Heat generated due to damping in the test specimen is equal to the heat absorbed in the test specimen plus heat removed from the surface of the test specimen by natural convection, so:

$$\rho C\frac{dT}{dt} + 2h\frac{(w+d)}{wd}(T - T_{am}) = \pi f\tan(\delta)(\frac{\sigma^2}{E}) \tag{16}$$

where t is time, ρ is the material density, C is the specific heat capacity, f is the frequency of the fatigue test, w is width and d is thickness of the test specimen, respectively, T_{am} is the ambient temperature and h is the natural convection heat transfer coefficient. The heat transfer coefficient h has been calculated by using the Nusselt number, Nu:

$$h = \frac{\mathrm{Nu}l}{K} \tag{17}$$

where l is the length of the test specimen and K is the conductivity of air. The Nusselt number is dependent on the Rayleigh and Prandtl numbers (Ra and Pr, respectively) and for engineering applications, the following relationship can be used based on vertical plates [31]:

$$\mathrm{Nu} = (0.825 + \frac{0.387\mathrm{Ra}^{\frac{1}{6}}}{[1 + (0.492/\mathrm{Pr})^{\frac{9}{16}}]^{\frac{8}{27}}})^2 \tag{18}$$

where the Rayleigh number is given by:

$$\mathrm{Ra} = \frac{g\beta(T_s - T_{am})l^3}{\nu\alpha}, \quad T_s = \frac{T_i + T_f}{2} \tag{19}$$

where g is gravitational acceleration, and β, ν and α are the thermal expansion coefficient, kinematic viscosity and thermal diffusivity of air, respectively. T_s is the surface temperature of the test specimen based on an average during the fatigue test where T_i and T_f are the initial and final surface temperatures, respectively. The Prandtl number is defined as:

$$\mathrm{Pr} = \frac{\nu}{\alpha} \tag{20}$$

Solving Eq. (16), the temperature T is obtained:

$$T = \frac{b}{a} + (T_{am} - \frac{b}{a})e^{-a(t-t_0)}, \quad a = \frac{2h(w+d)}{wd\rho C}, \quad b = \frac{\pi f\tan(\delta)(\frac{\sigma^2}{E})}{\rho C} + \frac{2h(w+d)T_{am}}{wd\rho C} \tag{21}$$

Where t_0 is the time at the start of the fatigue test. Eq. (21) can then be used to relate the temperature T of the test specimen to the loss factor.

4. Experiments

In this section, firstly a description is given of the testing methodology and the test specimen which was used to represent a joint seen in a blade. Then, the experimental set-up is described which was used to analyse changes to the stiffness and damping properties of the specimens during a fatigue test.

4.1. Testing methodology

The testing methodology was based on previous work using an asymmetric three-point bending fatigue test of a Henkel beam, representative of a spar to shear web assembly of a wind turbine blade [2]. This bending test indicated that damage progresses on the upper spar face of the beam which is under tension. This test showed that damage began with transverse cracks in the bond-line of the upper spar to shear web of the beam and when the cracks reached the saturation state, damage progressed to de-bonding and final failure of the beam. In the

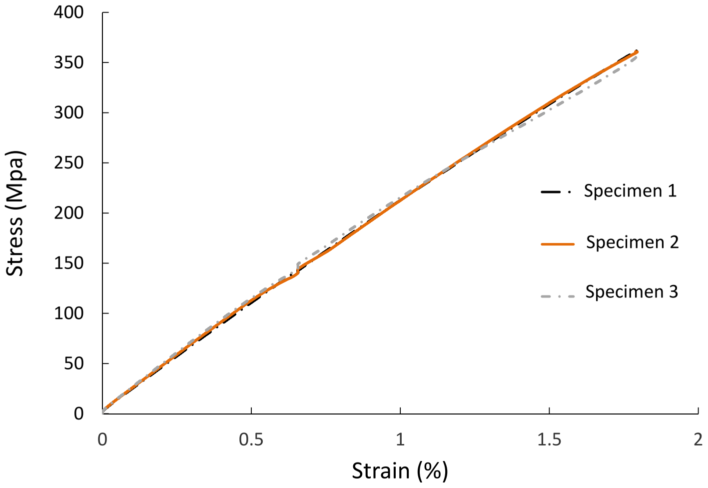

Fig. 3. Ultimate tensile test for the three test specimens..

lower spar face of the beam, no damage was observed until instability occurred in the final stage of failure. Moreover the transverse shear stress component was about 10% of the normal tensile stress component. This suggested that a simple fatigue tension test can provide a realistic assessment of incipient damage in a web adhesive joint present in a wind turbine blade. The use of a simple small test specimen to represent the joint has the advantage that manufacturing flaws can be minimised ensuring that results are consistent and accurate.

Several test specimens were manufactured for the experiment. Each test specimen consisted of two skins of unidirectional fibre glass which were made by the infusion of epoxy resin into three layers of unidirectional (UD(0)) fibres. These two skins were then bonded together by a layer of adhesive. The material properties of all components for manufacturing the test specimens are given inTable 1 and a schematic illustration of a test specimen is shown in Fig. 2.

To apply the correct load amplitude during the fatigue tests, the ultimate strength of several of the test specimens was identified by means of ultimate tensile strength tests. The results for three test specimens are shown in Fig. 3. The average value of the ultimate tensile strength and Young's modulus of the specimens was found to be 365 MPa. and 20.1 GPa, respectively.

4.2. *Experimental set up*

Three test specimen were subjected to a tension fatigue test using a 100 KN hydraulic fatigue rig under the load control condition as illustrated in Fig. 4. Fig. 4(a) shows the real-life set-up and Fig. 4(b) shows a schematic representation of the modal test set-up. Before the start of each fatigue test, a modal test was carried out on the healthy test specimen using an automatic hammer to excite the specimen and a laser vibrometer connected to a data acquisition system to record the vibration data. After a specified number of cycles, the fatigue test was halted and a further vibration test was carried out. This was repeated several times to build up a time-line of vibration response during progressive fatigue damage.

The purpose of the modal tests was to determine the experimental FRF of each test specimen. In conjunction with an analytical form of the FRF, as described in Section 3.1, it was then possible to determine the stiffness and damping properties of the specimen.

To calculate the damping using thermography, a FLIR A655sc type infrared camera was used. The camera is equipped with an uncooled Vanadium Oxide (VoX) microbolometer detector that produces thermal images of 640 x 480 pixels. The device is capable of detecting temperature differences as small as $50mK$. The temperature of each test specimen is continuously measured during the fatigue life and the increase in temperature is correlated to the heat generated inside the test specimen to estimate the loss factor as described previously.

5. Results

In this section, we first present the damage propagation observed during the fatigue tests. Then we determine the stiffness and damping properties of the thick adhesive joint for different levels of damage.

5.1. *Damage evolution in the adhesive joint*

Each test specimen was subjected to a fatigue tension test with the stress ratio, R (ratio of minimum load amplitude to maximum load amplitude) equal to 0.1, a fatigue cycling frequency of 3 Hz and a progressive maximum load amplitude as shown in Fig. 5. After around 1.3×10^4cycles, the first cracks appeared in the adhesive joints.

As cracks occurred in the adhesive, delamination appeared simultaneously in the vicinity of the crack point in the laminate. This can be considered as the first damage phase (I). As the depth of the cracks through the adhesive increased, so did the area of de-lamination. This trend continued until the cracks reached the saturation phase where the crack density was 66.7 m^{-1}. During the damage saturation phase (II), due to increase in the crack depth and de-lamination area, debonding of the adhesive from the face-sheets in the vicinity of some crack points took place. The initially limited number of de-bonded areas increased and became widespread throughout the test specimen. In the final phase of damage (III), these disconnected de-bonded areas became linked together and led to the final failure of the test specimen. The progressive phases of damage as a function of load cycle are shown in Fig. 5. The crack density versus the number of fatigue cycles during the three different phases of damage for the three test specimens (samples) are shown in Fig. 6. The three specimens show relatively consistent results with a small amount of spread.

5.2. *Stiffness measurement*

During the different phases of damage, the fatigue test was halted and the stiffness was measured using an extensometer. The results are shown in Fig. 7. Noticeably, there is more spread in the stiffness values for the three specimens compared to the crack density. In the first phase of damage, which corresponds to the initiation of the transverse cracks, there was no significant change in the stiffness. During the crack saturation phase, an average reduction of 4.7% in the stiffness was observed. The stiffness reduced while de-bonding was initiated and expanded and the test specimen experienced a total average reduction of 8.6% in stiffness before final failure.

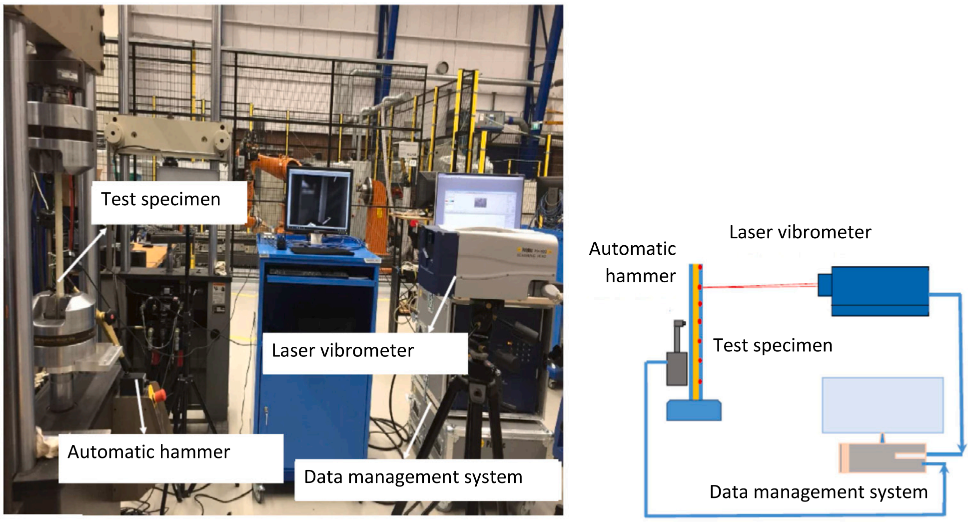

(a) (b)

Fig. 4. (a) Actual and (b) schematic of the experimental test set up to carry out the fatigue and modal tests.

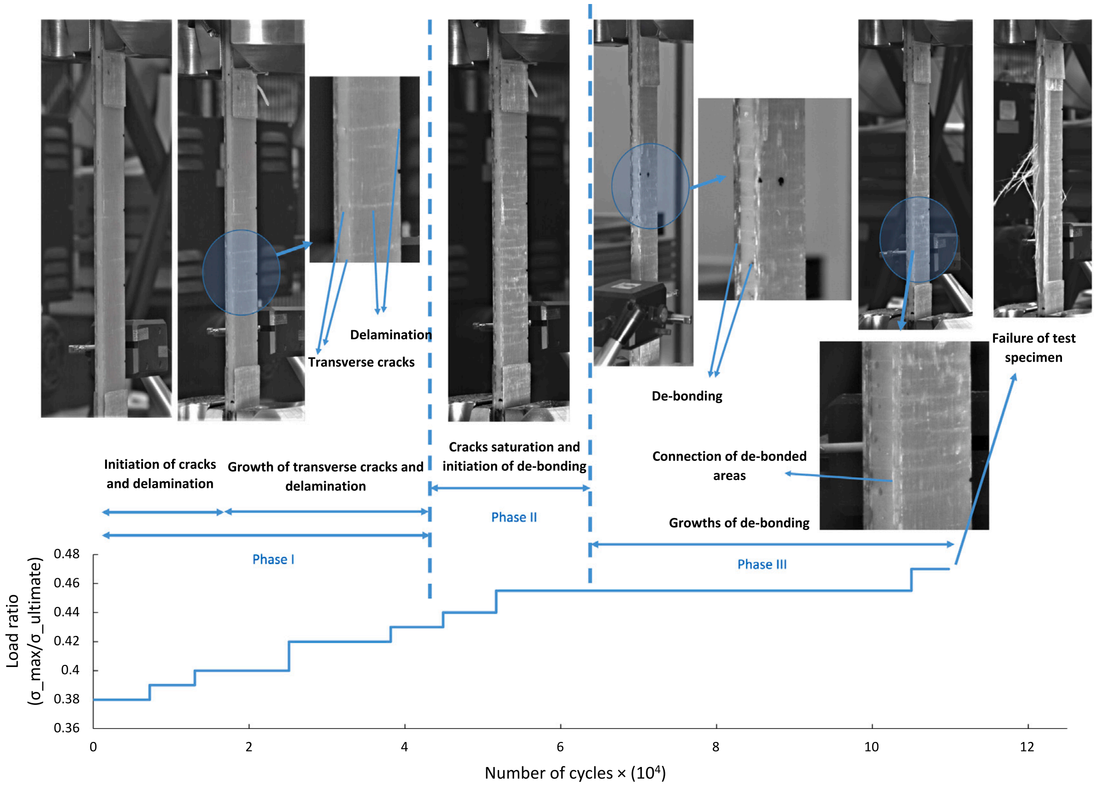

Fig. 5. Damage progression in one of the test specimens during the tension fatigue test. N.B. On the vertical axis, $\sigma_{\_max}$ and $\sigma_{\_ultimate}$ are the maximum stress amplitude of the fatigue test and the ultimate strength of the test specimen, respectively..

5.3. Calculation of the loss factor using the vibration method

Using Eq. (13), a best fit to the experimental data close to the first natural frequency is made of the GHM parametric form of the dynamic modulus by adjusting the model parameters. A comparison between the experimental FRF and theoretical FRF of one specimen is shown in Fig. 8(a). The best fit FRF for different levels of damage is shown in Fig. 8(b).

The best fit theoretical FRF is then used to calculate the loss factor for different levels of damage as shown in Fig. 9. The loss factor varies with the frequency with a maximum value near to the first natural frequency. The change in the value of the loss factor close to the first natural frequency for the three distinct phases of damage is shown in Fig. 10. It can be seen from this figure that in Phase I, as the number of cracks increases, the loss factor also increases. In the crack saturation state (Phase II), although the number of cracks does not change, the loss factor does increase due to growth in de-lamination. The average

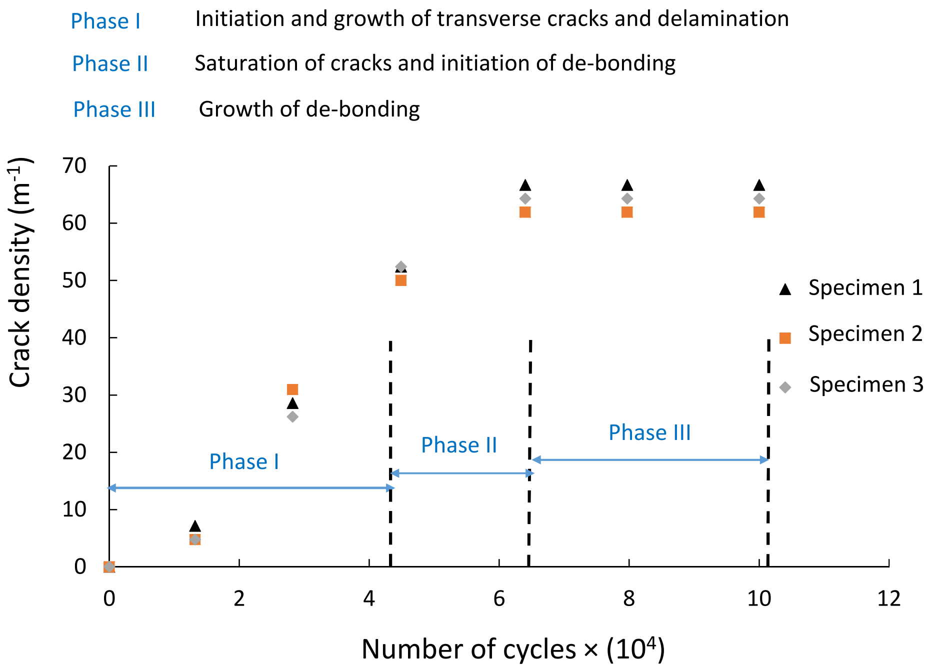

Fig. 6. Crack density versus fatigue load cycles during the different phases of damage throughout the fatigue test.

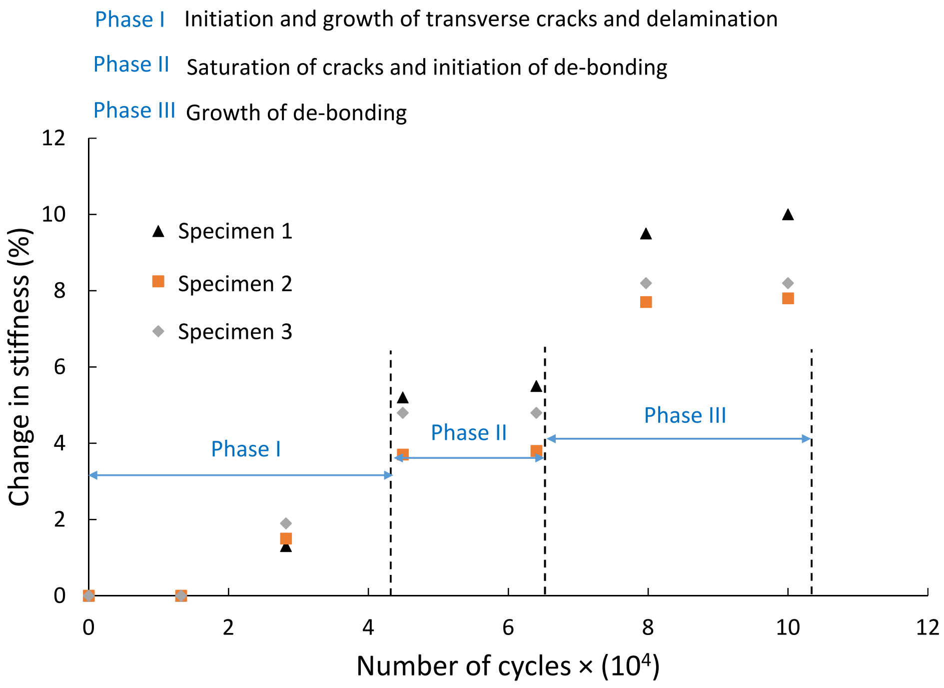

Fig. 7. Reduction in stiffness versus fatigue load cycles during different phases of damage.

cumulative change in the loss factor from initiation of cracks until crack saturation is 65.7%. In the third phase of damage, due to the increase in the depth of transverse cracks, the shear stress between the adhesive and the laminate increases leading to de-bonding of the adhesive from the laminate. The disconnected de-bonded areas become linked together and lead to the final failure of the test specimen. This mechanism seems to be the reason for the increase of the loss factor in this third damage region. An average cumulative increase in the loss factor of 111.4% is estimated before failure of the test specimen.

5.4. *Infrared thermography results*

Fig. 11 shows temperature maps measured using the infrared camera and pictures taken in visible light of one of the test specimens at different stages during the fatigue test.

The different stages of damage and their locations can be seen. The temperature increases during the fatigue test and after 1.5×10^4 cycles, the first sign of cracks can be seen by looking at local extremes of temperature (hot spots) shown by arrows in Fig. 11. As the fatigue test progresses, the number and temperature of the hot spots increases. This

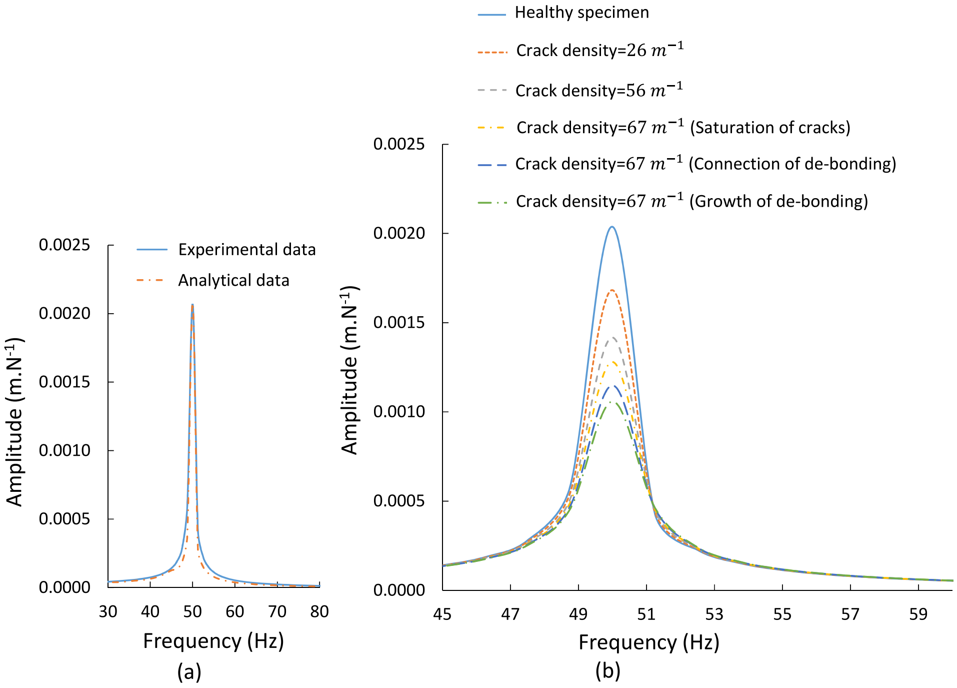

(a) (b)

Fig. 8. (a) Comparison of the theoretical and experimental FRF (b) The best FRF to data in the vicinity of the first natural frequency for different levels of damage.

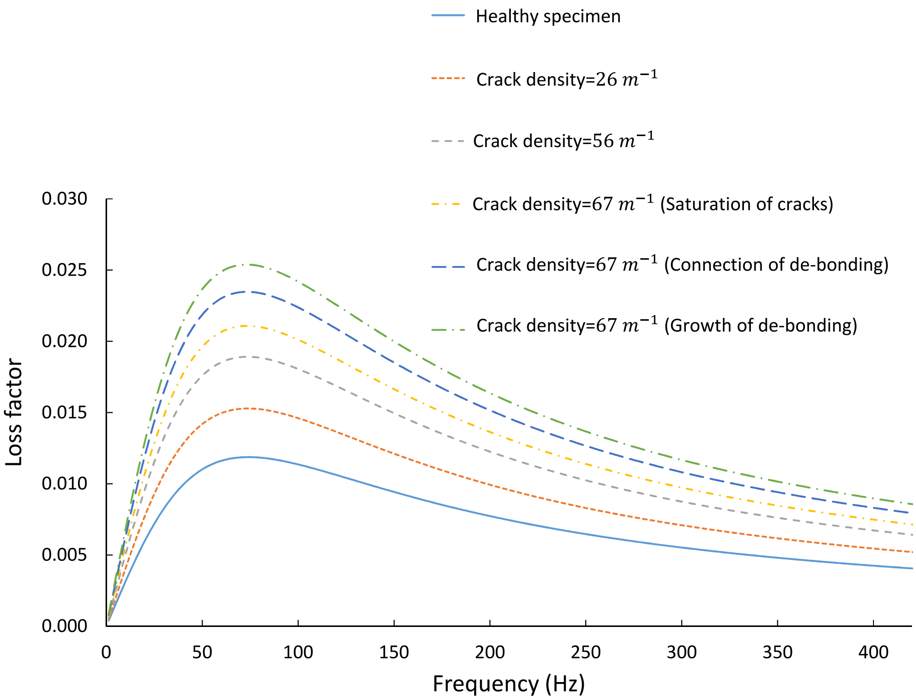

Fig. 9. Loss factor versus frequency for different levels of damage.

trend continues until 4.5×10^4 cycles when the number of hot spots is almost equally distributed throughout the length of the sample. This implies that the crack saturation phase (II) has been reached. As the number of load cycles increases, crack lengths increase and de-bonding of the laminate from the adhesive begins. This leads to an increase in temperature and wider hot spots.

To better illustrate the increase in the number of cracks until saturation occurs, the temperature profile across a line through the middle of a test specimen is plotted in Fig. 12. Local extremes in temperature indicate the locations of cracks which clearly grow in number and severity as the test progresses and the number of cracks reaches saturation. Again, the results presented are for one of the specimens, but the same trend is seen for all.

To calculate the damping, firstly the reference damping corresponding to the healthy test specimen is calculated. This can be done by fitting the loss factor to the average surface temperature of the test

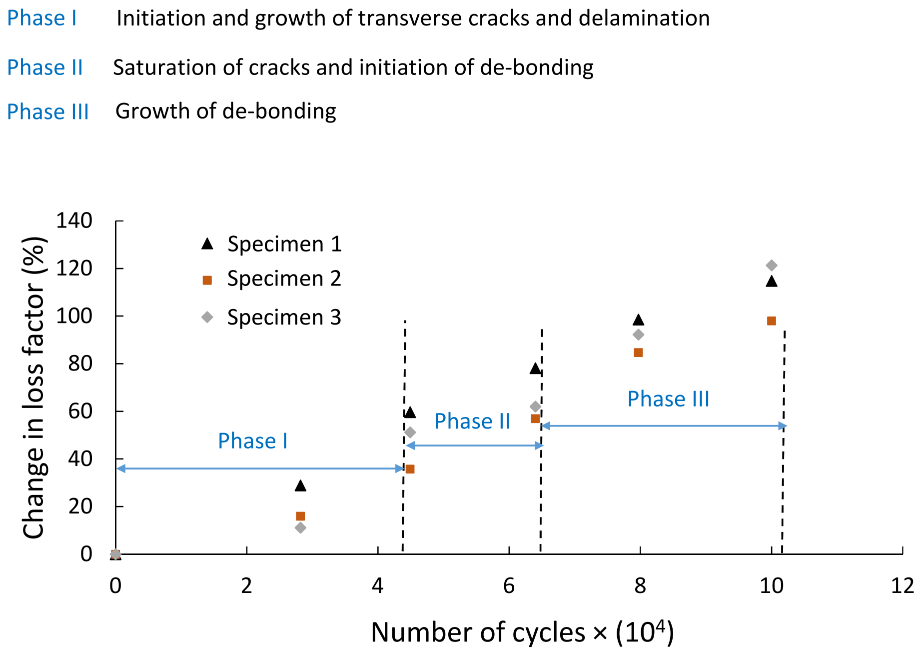

Fig. 10. Change in loss factor versus fatigue load cycles during the different phases of damage.

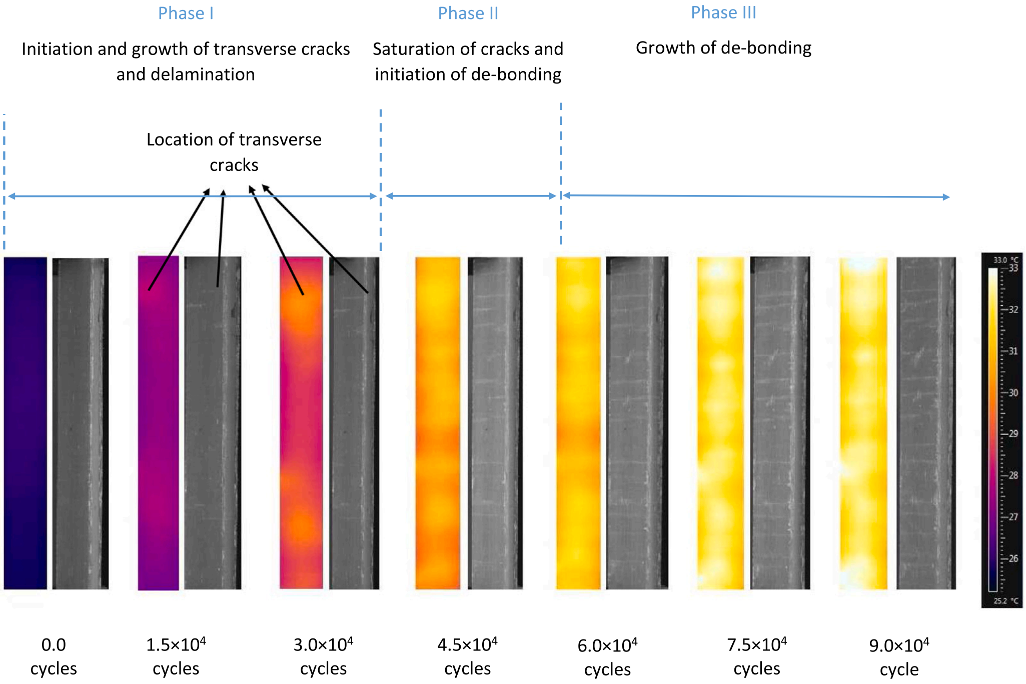

Fig. 11. Temperature of one of the test specimens at different stages of the fatigue test. Pictures taken in visible light are shown alongside for comparison.

specimen up until 2×10^4 load cycles during which little damage has occurred. The results of one test specimen has been shown in Fig. 13. During the first $2{\times}10^4$ load cycles, the specimen reaches an approximate steady state temperature of 28.3 °C where the heat generated in the test specimen is in balance with the heat removed from surface of test specimen by natural convection. The loss factor which gives the best fit to this measured temperature is about $\delta = 0.0013$.

Fig. 14 shows for the three test specimens the change in average temperature during the fatigue test. At the beginning of the test, the specimens rapidly heat up during the first 5000 cycles. A steady state temperature is then reached at around 2×10^4 load cycles as described above where little or no damage is seen. After this point a more rapid increase in temperature is seen as cracks are initiated during Phase I. The temperature rise slows during Phase II as crack saturation is reached. Finally, during the final Phase III where de-bonding and ultimate failure occurs the temperature profile flattens off.

Using the temperature values in Fig. 14 and the reference steady state temperature for the healthy specimen, the loss factor during the different phases of damage can be determined. These values are shown in Fig. 15.

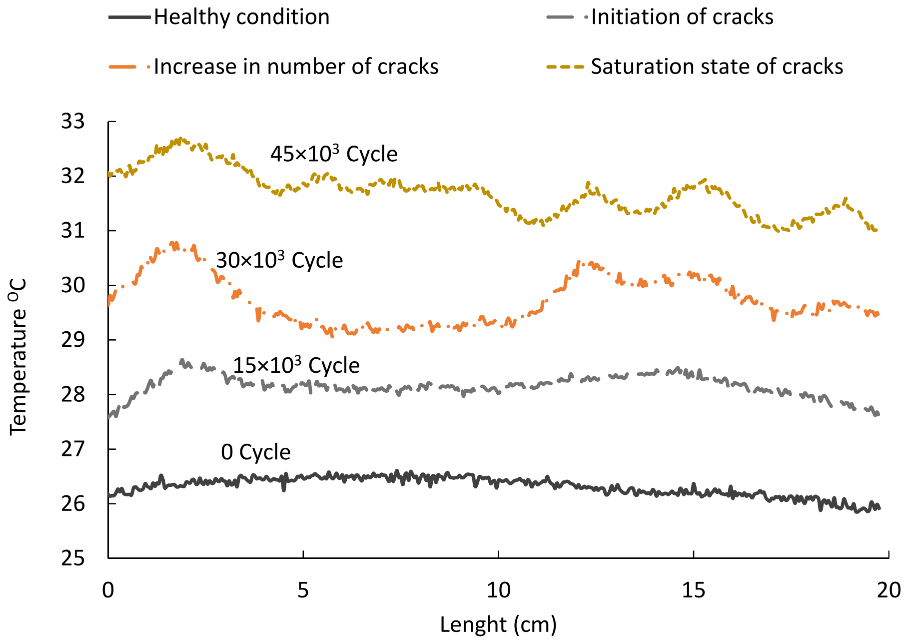

Fig. 12. Temperature profile across the mid-line of a test specimen at different stages of the fatigue test.

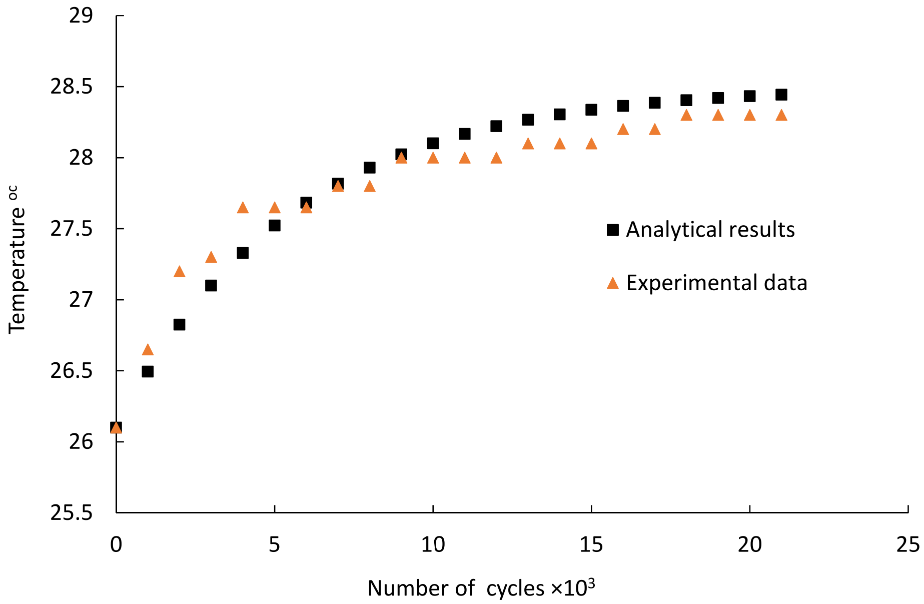

Fig. 13. Experimental and theoretically fitted temperature values based on thermographic measurements for an assumed healthy test specimen where $\delta = 0.0013$ and excitation frequency of $f = 3$ Hz.

5.5. Comparison between vibration and thermographic estimates of the loss factor

The results of the mean loss factor from the three specimens calculated using the vibration and the thermographic measurements are compared in Fig. 16. Two standard deviations are also shown based on the three specimens. Both methods show an increase in the change of loss factor during the different stages of the fatigue life. Initially, the match is good though once crack initiation accelerates during Phase I, there is a divergence in the estimate of the increase in loss factor inferred by the two methods. This divergence is greatest during Phase II, however, there is degree of scatter in the results for the three specimens. The results of the two methods converges close to the end of the fatigue life of the specimens.

It is clear that both methods are capable of detecting changes in the damping properties of the adhesively bonded joints, albeit with some divergence in the absolute values during the middle of the fatigue life. Additionally, the thermographic technique has the advantage of being able to localise damage. Having two independent techniques to assess changes in damping can give an improved measure of uncertainty, though the difference observed requires further investigation.

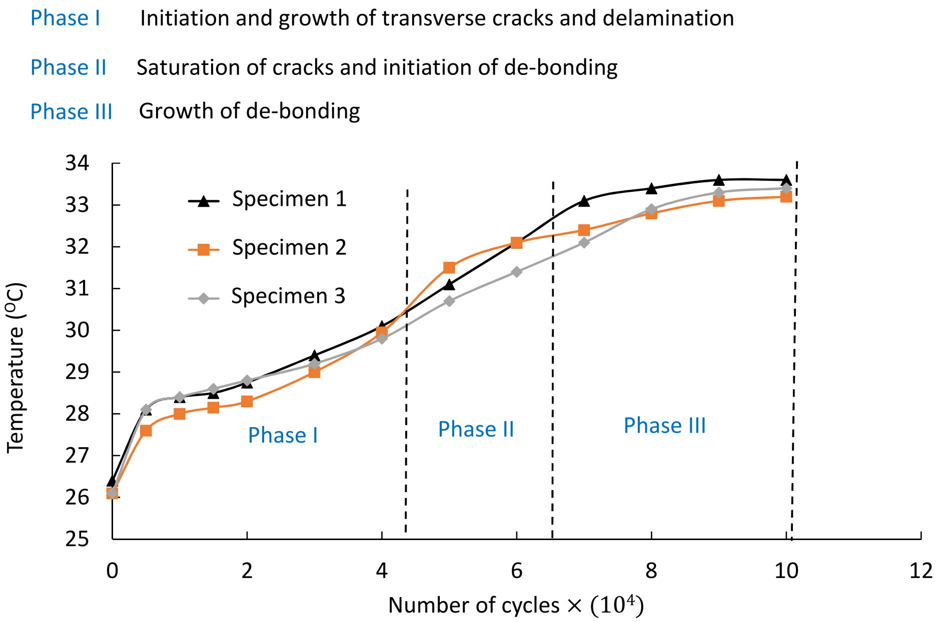

Fig. 14. Average surface temperature of the test specimen during its fatigue life.

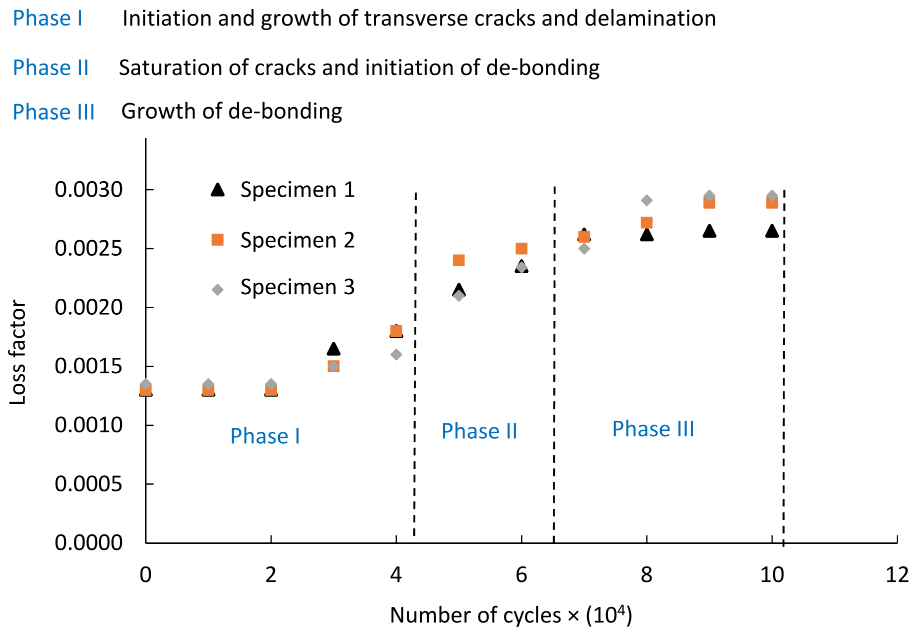

Fig. 15. The loss factor during the fatigue tests for the three test specimens inferred from thermographic measurements.

6. Discussion and conclusion

In this study, changes in the stiffness and damping properties of a thick adhesive joint during different phases of damage have been studied. Damping has been calculated using vibration and thermographic techniques. The results of these techniques are consistent in detecting trends although absolute values differ in the middle of the fatigue life. The thermographic technique has the advantage that it can also be used to identify the location of early cracks. In the damage initiation phase (Phase I), the relative change in the stiffness is small (less than 2%) but the change in the average loss factor is 18.6% and 17.8% using the vibration and thermographic methods, respectively. In the crack saturation phase (Phase II), the reduction in the stiffness is only 4.7% but there is a considerable increase in loss factor of about 65.7% and 95.6% using the vibration and thermographic methods, respectively. In the de-bonding phase of damage (Phase III), the stiffness reduces by 8.6% overall while the loss factor reduces substantially by 111.4% and 116.9% using the vibration and thermographic methods, respectively. It can be concluded that changes to the material damping properties of an adhesive joint representative of that in a wind turbine blade are more sensitive to damage than changes in stiffness and could be used in the condition monitoring of a blade. Further work would be required to determine how such changes could be used in a functioning monitoring system incorporating the use of vibration and thermographic methods.

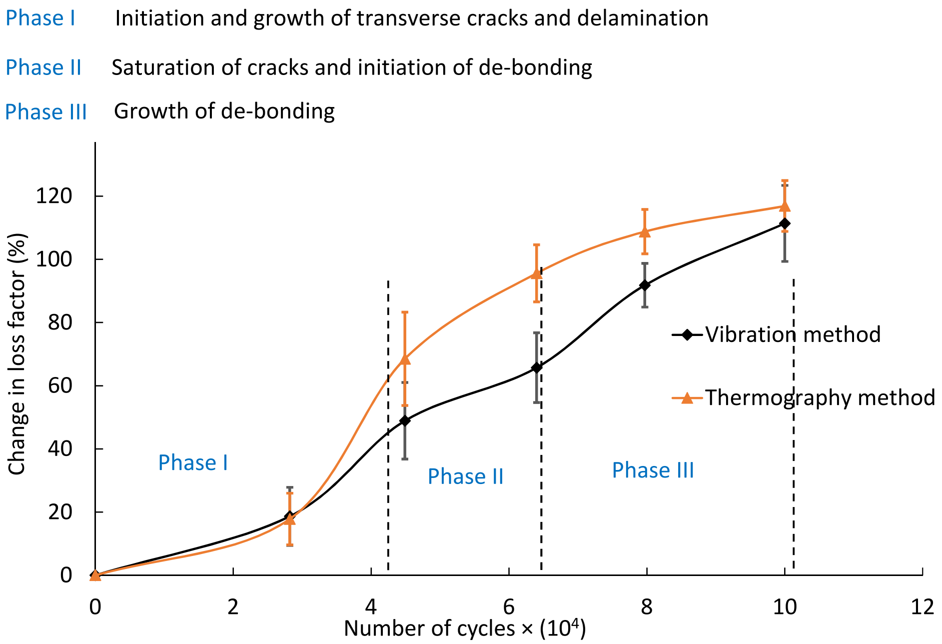

Fig. 16. Comparison of loss factor calculated using vibration and thermographic methods based on the three test specimens. Mean and two standard deviations are shown.

CRediT authorship contribution statement

S. Khoshmanesh: Conceptualisation, Methodology, Investigation, Acquisition of data, Formal analysis, Interpretation of data, Validation, Writing – original draft, Writing – review & editing, Resources (Provision of laboratory samples), Project administration. **S.J. Watson:** Conceptualisation, Methodology, Interpretation of data, Validation, Writing – review & editing, Supervision, Project administration. **D. Zarouchas:** Conceptualisation, Methodology, Interpretation of data, Validation, Writing – review & editing, Supervision, Project administration.

Declaration of competing interest

The authors declare that they have no known competing financial interests or personal relationships that could have appeared to influence the work reported in this paper.

Acknowledgments

All experimental tests were conducted in the structure laboratory at the Aerospace Faculty of the Delft University of Technology (TU Delft). The authors would like to thank the laboratory staff for their support during these experiments.

References

[1] Zarouchas D, Makris A, Sayer F, van Hemelrijck D, van Wingerde A. Investigations on the mechanical behavior of a wind rotor blade subcomponent. Compos Part B: Eng 2012;43:647–54. http://dx.doi.org/10.1016/j.compositesb.2011.10.009.

[2] Sayer F, Antoniou A, van Wingerde A. Investigation of structural bond lines in wind turbine blades by sub-component tests. Adhesion Adhesives 2012;37:129–35. http://dx.doi.org/10.1016/j.ijadhadh.2012.01.021.

[3] Wenxian Y, Tavner P, Crabtree C, Feng Y, Qiu Y. Wind turbine condition monitoring: technical and commercial challenges. Wind Energy 2014;17:673–93. http://dx.doi.org/10.1002/we.1508.

[4] Hu B, Stumpf P, van der Deijl W. Offshore wind access. TNO report, 3rd ed.. 2019, Report no:R10633.

[5] Fischer K, Coronado D. Condition monitoring of wind turbines: State of the art, user experience and recommendations. VGB PowerTech 2015;2015:51–6.

[6] Li D, Ho MS, Song G, Ren L, Li H. Review of damage detection methods for wind turbine blades. Smart Mater Struct 2015;24:033001. http://dx.doi.org/10.1088/0964-1726/24/3/033001.

[7] Carden P, Fanning P. Vibration based condition monitoring: A review. Struct Health Monit 2004;3:355–77. http://dx.doi.org/10.1177/1475921704047500.

[8] Montalvao D, Maia M, Ribeiro R. A review of vibration-based structural health monitoring with special emphasis on composite materials. Shock Vib Digest 2006;38:295–324. http://dx.doi.org/10.1177/0583102406065898.

[9] Kong X, Cai CS, Hu J. The state of the art on framework of vibration based structural damage identification for decision making. Appl Sci 2017;7:497. http://dx.doi.org/10.3390/app7050497.

[10] Hoon S, Charles R, Farrar R, Francois H, Devin S, Daniel W, et al. A review of structural health monitoring literature: 1996– 2001. Los Alamos National Laboratory Report; 2004, LA-13976-MS.

[11] Doebling W, Farrar PM. Summary review of vibration-based damage identification methods. Shock Vib Digest 1998;30:91–105. http://dx.doi.org/10.1177/058310249803000201.

[12] Al-Khudairi O, Hadavinia H, Little C, Gillmore G, Greaves P, Dyer K. Full-scale fatigue testing of a wind turbine blade in flapwise direction and examining the effect of crack propagation on the blade performance. Materials 2017;10:1152. http://dx.doi.org/10.3390/ma10101152.

[13] Modena C, Sonda D, Zonta D. Damage localization in reinforced concrete structures by using damping measurements. Key Eng Mater -KEY ENG MAT. 1999;167–168:132–41. http://dx.doi.org/10.4028/www.scientific.net/KEM.167-168.132.

[14] Zonta D, Modena C. Observations on the appearance of dispersive phenomena in damaged structures. J Sound Vib 2001;241:925–33. http://dx.doi.org/10.1006/jsvi.2000.3320.

[15] Kawiecki G. Modal damping measurement for damage detection. Smart Mater Struct 2001;10:466–71. http://dx.doi.org/10.1088/0964-1726/10/3/307.

[16] Keye S, Rose M, Sachau D. Localizing delamination damages in aircraft panels from modal damping parameters. In: In Proc. 19Th international modal analysis conf(IMAC XIX). 2001, p. 412–7.

[17] Kyriazoglou C, Page B, Guild F. Vibration damping for crack detection in composite laminates. Compos Part A-Appl Sci Manuf 2004;35:945–53. http://dx.doi.org/10.1016/j.compositesa.2004.01.003.

[18] Zhang Z, Hartwig G. Relation of damping and fatigue damage of unidirectional fibre composites. Int J Fatigue 2002;24:713–8. http://dx.doi.org/10.1016/S0142-1123(01)00206-7.

[19] KiRal Z, Icten MB, Kiral GB. Effect of impact failure on the damping characteristics of beam-like composite structures. Composites B 2012;43:3053–60. http://dx.doi.org/10.1016/j.compositesb.2012.05.005.

[20] Birman V, Byrd L. Effect of matrix cracks on damping in unidirectional and cross- ply ceramic matrix composites. J Compos Mater 2002;36:1859–77. http://dx.doi.org/10.1177/0021998302036015247.

[21] Cao M, Sha G, Gao Y, Ostachowicz W. Structural damage identification using damping: a compendium of uses and features. Smart Mater Struct 2017;26:043001. http://dx.doi.org/10.1088/1361-665X/aa550a.

[22] Kopparthi PK, Aerra KKY, Pathakokila BR, Gamini S. Bending and viscoelastic behaviour of delaminated woven E-glass/epoxy composite. Aust J Mech Eng 2020;1–10. http://dx.doi.org/10.1080/14484846.2020.1794506.

[23] Shen Y, Tan J, Fernandes L, Qu Z, Li Y. Dynamic mechanical analysis on delaminated flax fiber reinforced composites. Mater (Basel) 2019;12(16):2559. http://dx.doi.org/10.3390/ma12162559.

[24] Khoshmanesh s, Watson SJ, Dimitrios Z. Characterisation of fatigue damage in a thick adhesive joint based on changes in material damping. J Phy: Conf Series 2020;1618:022058. http://dx.doi.org/10.1088/1742-6596/1618/2/022058.

[25] Gibson R. Damping characteristics of composite materials and structures. J Mater Eng Perform 1992;1:11–20. http://dx.doi.org/10.1007/BF02650027.

[26] Treviso A, Genechten VBBV, Mundo D, Tournour M. Damping in composite materials: Properties and models. Compos Part B-Eng 2015;78:144–52. http://dx.doi.org/10.1016/j.compositesb.2015.03.081.

[27] Sørensen FB, Holmes J, Brøndsted P, Branner K. Blade materials, testing methods and structural design. WIT Trans State–Art Sci Eng 2010;44:417–66.

[28] Mishnaevsky L, Branner K, Petersen H, Beauson J, Mcgugan M, Sørensen FB. Materials for wind turbine blades: An overview. Materials 2017;10. http://dx.doi.org/10.3390/ma10111285.

[29] Lakes Roderic. Viscoelastic materials. Cambridge University Press; 2009, http://dx.doi.org/10.1017/CBO9780511626722.

[30] McTavish JD, Hughes P. Modeling of linear viscoelastic space structures. J Vib Acoust 1993;115:103–10. http://dx.doi.org/10.1115/1.2930302.

[31] Frank INCROPERA P, DEWITT PD, Bergman LT, Lavine SA. Fundamentals of heat and mass transfer. John Wiley and Sons; 2007, 978-0-471-45728-2.